Linear pattern dynamics in nonlinear threshold systems

John B. Rundle
Department of Physics and Colorado Center for Chaos and Complexity and Cooperative Institute for Research in Environmental Sciences, University of Colorado, Boulder, Colorado 80309

W. Klein
Department of Physics and Center for Computational Science, Boston University, Boston, Massachusetts 02215

Kristy Tiampo and Susanna Gross
Colorado Center for Chaos and Complexity, Cooperative Institute for Research in Environmental Sciences, University of Colorado, Boulder, Colorado 80309

(Received 15 July 1999)

Complex nonlinear threshold systems frequently show space-time behavior that is difficult to interpret. We describe a technique based upon a Karhunen-Loeve expansion that allows dynamical patterns to be understood as eigenstates of suitably constructed correlation operators. The evolution of space-time patterns can then be viewed in terms of a ''pattern dynamics'' that can be obtained directly from observable data. As an example, we apply our methods to a particular threshold system to forecast the evolution of patterns of observed activity. Finally, we perform statistical tests to measure the quality of the forecasts.

PACS number(s): 02.50.Ey

I. INTRODUCTION

Driven nonlinear threshold system are comprised of interacting spatial networks of statistically identical, nonlinear units or cells that are subjected to a persistent driving force or current. A cell ''fires'' or ''fails'' when the force, electrical potential, or other physical variable $\sigma(\mathbf{x},t)$ on a cell at position $\mathbf{x}$ and time t reaches a predefined force threshold σ^F. The result is an increase in an internal state variable $s(\mathbf{x},t)$ of the cell, as well as a decrease in the force or potential sustained by the cell to a residual value σ^R. Thresholds, residual stresses, and internal states may be modified by the presence of quenched disorder. The dynamics may also be modified by the presence of noise or annealed disorder. Interactions between cells may be excitatory (positive) in the sense that failure of connected neighbors brings a cell closer to firing or inhibiting (negative) in the opposite case. Examples of such systems include earthquakes [1–3], neural networks [4,5], depinning transitions in charge-density waves and superconductors [6], magnetized domains in ferromagnets [7], sandpiles [8], and foams [9]. Numerical simulations of these systems reveal spatial and temporal patterns of firings $\Psi(\mathbf{x},t)$ that are richly complex and difficult to understand from any deterministic point of view [10]. Understanding such patterns will increase our understanding of the physics of the systems themselves, since these space-time patterns are emergent processes that reflect the structures, dynamics, and properties of the underlying high-dimensional nonlinear system.

In a number of these driven threshold systems, there exists the further difficulty that the deterministic dynamics, together with values of the state variables $s(\mathbf{x},t)$, are often unknown or unobservable. However, the associated firing activity pattern variables $\Psi(\mathbf{x},t)$ *are* easily observable. It is important to note here that the space-time patterns in firing activity $\Psi(\mathbf{x},t)$ should not be confused with space-time patterns displayed by the variables in which the underlying dynamics is formulated, $s(\mathbf{x},t)$ and $\sigma(\mathbf{x},t)$. These latter variables can also be expected to display patterns and correlations, from which the patterns in firing activity $\Psi(\mathbf{x},t)$ ultimately arise. However, patterns in $s(\mathbf{x},t)$ and $\sigma(\mathbf{x},t)$ are not of interest to us here, since in the systems we consider they are effectively not observable.

The firing activity $\Psi(\mathbf{x},t)$ can be represented as a set of time series at all positions $\mathbf{x}$, with $\Psi(\mathbf{x},t)$ defined by $\Psi(\mathbf{x},t)=1$ if a firing event occurs between $\{t,t+\Delta t\}$; $\Psi(\mathbf{x},t)=0$ otherwise. The basic problem is illustrated in Fig. 1. The state variable $s(\mathbf{x},t)$ at position $\mathbf{x}$ and time t evolves to a value $s(\mathbf{x},t+\Delta t)$ under the action of the deterministic dynamics D_t:

$$D_t\{s(\mathbf{x},t)\}\rightarrow s(\mathbf{x},t+\Delta t). \tag{1}$$

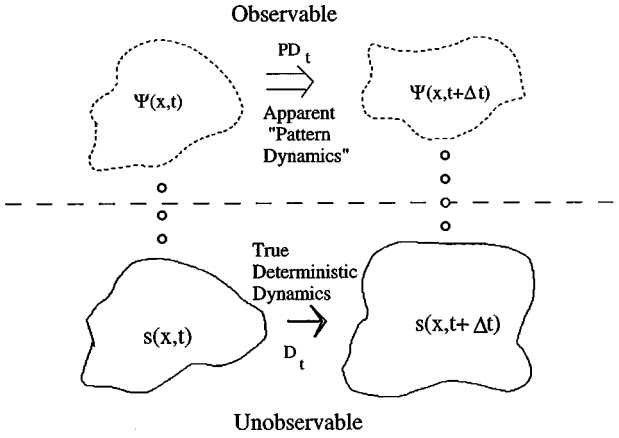

FIG. 1. Schematic diagram of threshold systems, including unobservable state variables $s(\mathbf{x},t)$ and observable pattern variables $\Psi(\mathbf{x},t)$.

The force or potential $\sigma(\mathbf{x},t)$ associated with $s(\mathbf{x},t)$ also evolves to $\sigma(\mathbf{x},t+\Delta t)$.

The values of $s(\mathbf{x},t)$ and $\sigma(\mathbf{x},t)$, together with details of the dynamics D_t, are usually hidden from view, below the horizontal dashed line in Fig. 1. For example, it is not possible to have simultaneous knowledge of all the cellular potentials of all neurons in a living brain at all times *t*, nor is it known what dynamical details govern the temporal evolution of the potentials and currents in all cells. Another example is the stress and strain at every point within the earth along active earthquake fault systems. There exists no means at present to observe values for these variables everywhere at time *t*, as would be needed to understand details of the dynamical processes that lead to earthquakes. While models for such dynamics exist, it is not clear how accurately these represent reality, since they have not been demonstrated to be useful in reliable earthquake forecasting.

By contrast, examples of observable ''firing'' activity include the firing patterns in groups of neural cells [11–14], which can be measured via remotely sensed electrical neural probes, as well as earthquakes, which can be located in space and time to reasonable precision using seismographs [15–17]. Since both $\Psi(\mathbf{x},t)$ and $\Psi(\mathbf{x},t+\Delta t)$ are observable, it might be possible in principle to learn about D_t, $s(\mathbf{x},t)$, and $\sigma(\mathbf{x},t)$ by studying the evolution of patterns. Unfortunately, there exists no evidence at present that $\Psi(\mathbf{x},t)$ is uniquely related to $s(\mathbf{x},t)$ and $\sigma(\mathbf{x},t)$. In other words, there may be a large number of states $s(\mathbf{x},t)$ that produce a similar pattern $\Psi(\mathbf{x},t)$, or a large number of patterns $\Psi(\mathbf{x},t)$ associated with similar states $s(\mathbf{x},t)$. This weak association between $s(\mathbf{x},t)$ and $\Psi(\mathbf{x},t)$ is represented schematically in Fig. 1 by a vertical dotted line.

In attempting to forecast the future evolution of driven threshold systems, the most common approach is to (1) use observations of $\Psi(\mathbf{x},t)$ to infer $s(\mathbf{x},t)$; then (2) use $s(\mathbf{x},t)$ together with an assumed model for the dynamics D_t to calculate $s(\mathbf{x},t+\Delta t)$; and finally (3) use $s(\mathbf{x},t+\Delta t)$ to infer $\Psi(\mathbf{x},t+\Delta t)$, which represents the observable pattern of interest. However, this method involves a long chain of inference and assumption, particular links of which may not be well justified. In an alternative approach, we propose the construction of an approximate dynamics based on Karhunen-Loeve (KL) methods that associate a future pattern state $\Psi(\mathbf{x},t+\Delta t)$ with an earlier pattern state $\Psi(\mathbf{x},t)$ by means of an assumed ''pattern dynamics'' operator $\mathcal{P}(D_t)$:

$$\mathcal{P}(D_t)\{\Psi(\mathbf{x},t)\}\Rightarrow\Psi(\mathbf{x},t+\Delta t). \tag{2}$$

Moreover, we propose to construct $\mathcal{P}(D_t)$ without any knowledge of the true deterministic dynamics D_t, using only knowledge of the pattern states preceding $\Psi(\mathbf{x},t)$.

The pattern dynamics operator that we construct operates on a space of functions $\Psi_R(\mathbf{x},t)$ that we call ''reconstructed pattern states.'' The $\Psi_R(\mathbf{x},t)$ are continuous in time and represent approximations, in the sense described below, to the pattern states $\Psi(\mathbf{x},t)$. In fact, the $\Psi_R(\mathbf{x},t)$ will be seen to represent probability amplitudes from which probability density functions for firing activity may be calculated. In contrast to the underlying deterministic dynamics D_t, which are most probably strongly nonlinear, the operator $\mathcal{P}(D_t)$ is assumed to be linear over small time intervals Δt. A convenient analogy for the relationship between $\mathcal{P}(D_t)$ and D_t is the correspondence between an equilibrium dynamical system, such as an Ising model that is governed by a nonlinear Langevin equation and the corresponding functional Fokker-Planck equation [18,19]. Evolution of dynamical variables, such as the spin density, is governed by a strongly nonlinear Langevin equation, but the probability density functions evolve according to a linear functional Fokker-Planck equation.

The assumption of a linear dynamics governing the $\Psi_R(\mathbf{x},t)$ follows from the statistical time-stationary properties of the underlying dynamics, which in turn justifies the use of methods based upon a Karhunen-Loeve expansion. We have shown in previous work [20–22] that mean-field threshold systems, characterized by long-range interactions between sites $\mathbf{x}$ and $\mathbf{x}'$, can be treated as equilibrium systems and have dynamics that are statistically stationary over long time intervals. These long intervals are eventually punctuated by rare, large events that serve to reorder the entire system. As the range of interaction increases, these equilibriumlike time intervals increase. In the limit of infinite range interactions where mean-field conditions hold and the system is ergodic, Poincaré's theorem [23] implies that dynamical variables can be written as sums and integrals of complex exponentials. In the work described here, we will construct a pattern dynamics for these mean-field systems.

Our approach is similar in some respects to previous ones that use correlation methods [10,25,26], but also has important differences. In most of these methods, a formalism is constructed that in effect uses space-time patterns to extrapolate future system behavior. However, our approach differs in that we retrieve a complete set of space-time patterns represented by the eigenvectors $\phi_n(\mathbf{x}_i)$ and eigenfrequencies ω_n of an equal time, rate-rate correlation function. The $\phi_n(\mathbf{x}_i)$ provide information about spatial correlations of patterns, whereas the ω_n provide information regarding how often each spatial correlation (eigenvector) is represented in the observed data. If the process is statistically stationary, as we have established for the mean-field threshold systems we consider, these $\phi_n(\mathbf{x}_i)$ and ω_n *will themselves be independent of time*. Hence $\phi_n(\mathbf{x}_i)$ and ω_n can justifiably be determined from an equal time correlation operator. From these eigenvectors and eigenfrequencies, as well as initial-value data on the most recent ''firing'' activity at each spatial location, we obtain the reconstructed pattern state $\Psi_R(\mathbf{x},t)$, which in turn is used to compute a probability density function $P(\mathbf{x},t)$.

Forecasting the future evolution of other nonlinear systems, such as climate, weather, or El Nino–southern oscillations, often involves the computation of an unequal time correlation function (UTC) over short time intervals [26–33]. However, in these systems, which are not ''threshold systems'' in the sense we consider here, the state variables $s(\mathbf{x},t)$ and force variables $\sigma(\mathbf{x},t)$ that define the true deterministic dynamics *can* be directly observed. These include wind speeds, temperatures, pressures, and so forth. The dynamics, as represented by the Navier-Stokes equation, are essentially known. In the case of earthquakes however, it would not be useful to construct a UTC operator for the state variables $s(\mathbf{x},t)$ and $\sigma(\mathbf{x},t)$, since the corresponding field variables (stresses and displacements on faults) are effec-

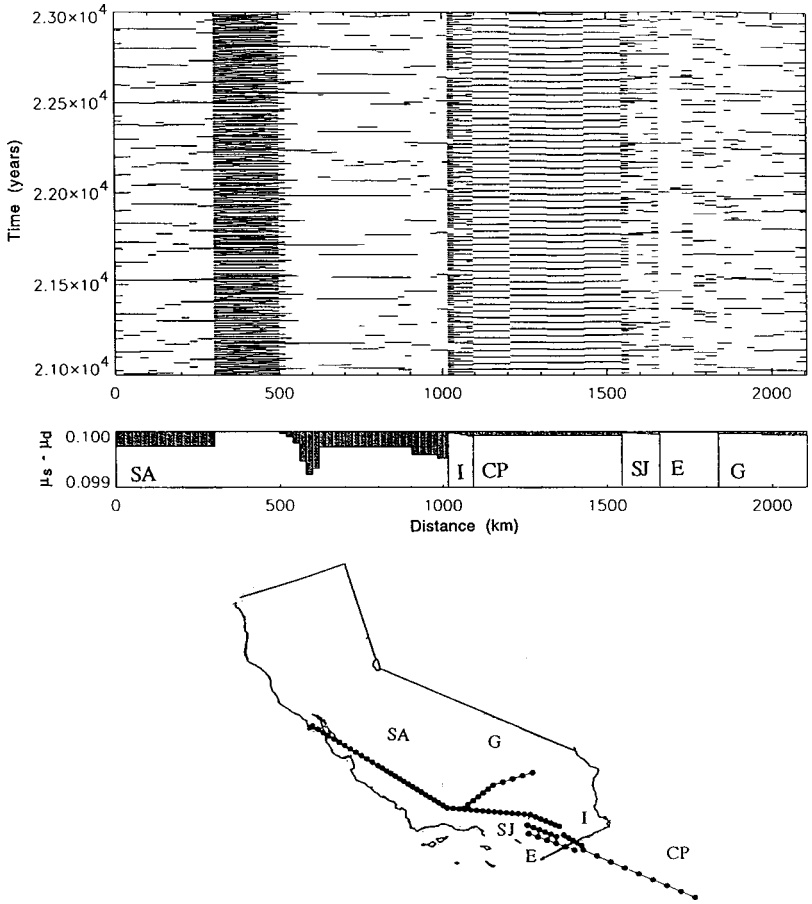

FIG. 2. (Top) time-distance plot of simulated seismic activity. $N=80$ fault segments (abbreviations in text) are plotted end to end, with north to left in all cases. The horizontal line over a given segment represents the slip of that segment at the time indicated. (Middle) plot of difference in friction coefficients $\mu_s-\mu_d$ as a function of distance along faults. (Bottom) map view of fault segments shown superimposed on a map of California. A segment is represented by the interval between dots.

tively unobservable. In addition, computing a UTC operator in the pattern variables $\Psi(\mathbf{x},t)$ is problematic because of the nature of the quiescent intervals. Long periods of activity are punctuated by short bursts of activity, making the definition of one or more time steps for the UTC problematic.

Our first attempts at forecasting the patterns seen in the earthquake simulations described below used just such a UTC technique, which is based on a linear operator acting on a state at time t to predict a state or probability at time $t+\Delta t$. As a result, the UTC forecast method is inherently unable to distinguish between the long-term quiescence that precedes a large earthquake mainshock and the quiescence that follows it. During the foreshock-mainshock-aftershock sequence, it is true that the probability of an earthquake of *any* size in the source region remains high. However, when viewed over the entire earthquake cycle, the probability of the earthquake mainshock should clearly be greater in the years leading up to the mainshock sequence than in the years following. Moreover, there is often a wide spectrum of time scales among the pattern states, a property that is extremely difficult for a method using a one-time-step UTC state transition matrix to adequately capture. For these reasons, our attempts at forecasting simulated earthquakes using an unequal time correlation operator were not satisfactory, and we were thus motivated to develop the method described in the following.

II. EXAMPLE: DYNAMICS AND ''PATTERN DYNAMICS''

Figure 2 illustrates space-time patterns of activity produced by a realistic earthquake fault model [34]. In this model, 80 fault segments are endowed with static and kinetic coefficients of friction, and are driven by a persistently increasing shear stress that, over long time intervals, produces slip events whose time-averaged rate of slip is equal to that observed in nature. In the model, there are six major faults: the San Andreas (SA), Imperial (I), Cerro Prieto (CP), San Jacinto (SJ), Elsinore (E), and Garlock (G). The top diagram is a plot with positions on all six faults concatenated together along the horizontal axis and with event times (lines) on the vertical axis for a simulation run. The middle diagram is a plot of friction against position, and the bottom is a map view of the faults. For this simulation, the coarse-grained time interval $\Delta t=1$ year. Details are given in Appendix B.

Referring to the top diagram in Fig. 2, each horizontal line represents an earthquake that occurred at the time indicated on the vertical axis. These data correspond to the observable patterns $\Psi(\mathbf{x},t)$ described above. At each position $\mathbf{x}_i$ along the earthquake faults, an activity time series can be constructed for which $\Psi(\mathbf{x}_i,t)=1$ if an earthquake occurs at time t, and $\Psi(\mathbf{x}_i,t)=0$ otherwise. Thus we have 80 time series, one for each fault segment, and each with 2000 time entries (2000 years in the simulation). These data are meant

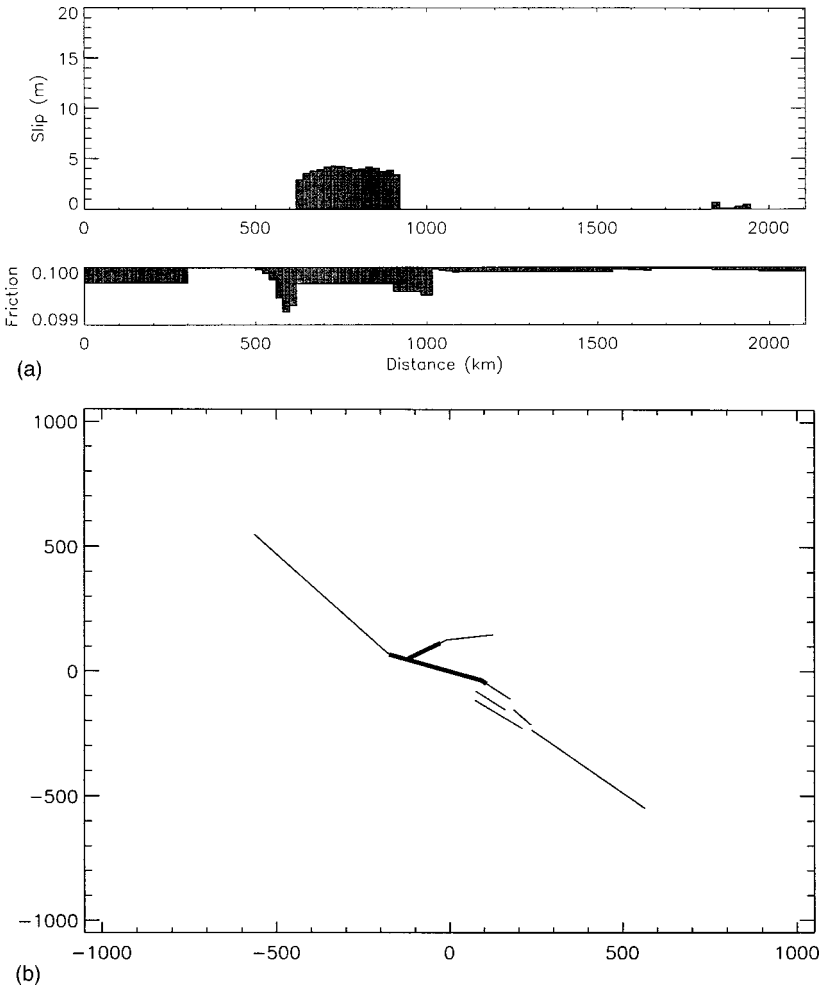

FIG. 3. Events at year (time step) 21 664. (a) Slip plotted against distance. (b) Map view of events.

to be a relatively realistic representation of actual seismic events. Like the real faults, the function $\Psi(\mathbf{x},t)$ represents the observable data and encodes all space-time patterns that may exist. In contrast, there are many unobservable parameters in the simulations. As described in Appendix B, each fault segment has coefficients of friction, a slip state variable, two stress variables (shear and normal stress), and so forth. In the real earth, at present there is no realistic possibility of measuring values for these variables.

III. BASIC METHOD

Viewed over the long time spans of hundreds to thousands of years characteristic of the earthquake cycle, it has long been observed that earthquake mainshocks are recurrent at quasiperiodic intervals [3]. For example, in the Nankai Trough near southwest Japan, the average interval between mainshocks is 180 ± 67 years. For the San Andreas fault at Pallet Creek in the Big Bend region of southern California, the interval is 131 ± 10 years. Elsewhere along the San Andreas, deviations from the mean are more significant [3]. At the famous Parkfield, California site, as well as along the Alaska-Aleutian trench, and along the central and South American subduction zones, average recurrence intervals are also well defined. However, temporal and spatial clustering is also evident in these data, as has been discussed elsewhere [3,35–38]. Analysis in Refs. [36,37] suggests that neither the recurrent nature of the mainshocks, nor the observed spatial-temporal clustering of activity is compatible with a Poisson probability function.

Nevertheless, if we were to attempt the construction of a probability density function $P(\mathbf{x}_i,t)$ to forecast an earthquake mainshock on any of these fault segments $\mathbf{x}_i$, a plausible approach would be to measure the average frequency of mainshock events on $\mathbf{x}_i$ by calculating

$$\omega_i=\pi\nu_i=\pi\left\{\frac{\text{number of events on } i\text{th segment}}{\text{time interval}}\right\} \quad (3)$$

and then write

$$P(\mathbf{x}_i,t)=Z_i^{-1}\{\cos\omega_i(t-t_0)\}^2. \quad (4)$$

The constant t_0 would be determined as the time of the latest slip event, and Z_i is a normalizing factor. It is important to emphasize that Eq. (4) refers to the probability of a mainshock, not to the foreshocks and aftershocks in the source region. This and other approaches have been examined in the literature [10–14,39–48], but success has so far been mixed.

The lack of success of present approaches has motivated our search for an alternative method in which $P(\mathbf{x}_i,t)$ is constructed by taking account of the variability in the data,

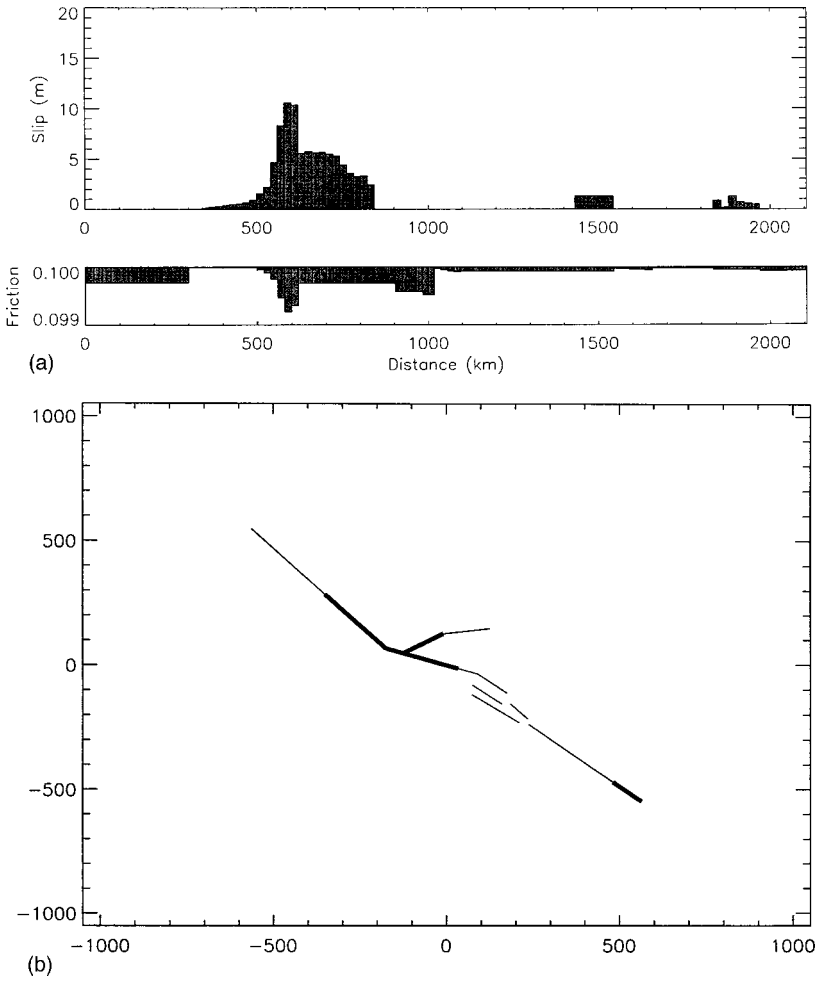

FIG. 4. Events at year (time step) 22 554. (a) Slip plotted against distance. (b) Map view of events.

as well as space-time correlations that may exist with activity at other sites $\mathbf{x}_j$. We have therefore developed a method based on a discrete Karhunen-Loeve expansion [24,25,27] that allows computation of the ''normal modes'' of the space-time pattern data from an equal-time correlation operator, yielding a set of eigenvectors $\phi_n(\mathbf{x})$ and a corresponding set of eigenfrequencies ω_n, $n=1,...,N$. If the process is statistically stationary, as has been established for the mean-field systems we consider, these $\phi_n(\mathbf{x})$ and ω_n *will themselves be independent of time*. Hence $\phi_n(\mathbf{x})$ and ω_n can justifiably be determined from an *equal time* correlation operator. It is important to stress that, due to the long-range nature of the stress transfer Green's function describing real faults, earthquake faults can be considered to be examples of mean-field systems.

In the case of Fig. 2, we have $N=80$ such eigenvectors and eigenfrequencies. From these, we compute the complex-valued, reconstructed pattern state $\Psi_R(\mathbf{x}_i,t)$:

$$\Psi_R(\mathbf{x}_i,t)=\sum_{n=1,N}\alpha_n e^{-i\omega_n t}\phi_n(\mathbf{x}_i). \tag{5}$$

The constants α_n are determined by fitting $\Psi_R(\mathbf{x}_i,t)$ to the time t_{0i} of the most recent slip event on segment $\mathbf{x}_i$, $\Psi_R(\mathbf{x}_i,t_{0i})=1$ [refer to Eq. (21) below]. Expression (5) can in principle describe phenomena in a system characterized by a large number of greatly diverse time scales $\tau_i=2\pi/\omega_i$.

From $\Psi_R(\mathbf{x}_i,t)$, we construct the real, observable part:

$$\Psi_{\mathrm{obs}}(\mathbf{x}_i,t)=\frac{1}{\sqrt{2}}\{\Psi_R(\mathbf{x}_i,t)+\Psi_R^*(\mathbf{x}_i,t)\}, \tag{6}$$

where $\Psi_R(\mathbf{x}_i,t)$ is written in terms of a sum of eigenvectors $\phi_n(\mathbf{x})$, which arise from an equal-time correlation operator. A correlation function is related to a probability density function. In this sense, $\Psi_R(\mathbf{x}_i,t)$ thus represents the ''square root'' of a probability, therefore a probability amplitude:

$$P(\mathbf{x}_i,t)=|\Psi_{\mathrm{obs}}(\mathbf{x}_i,t)|^2=\{\Psi_{\mathrm{obs}}(\mathbf{x}_i,t)\}^2. \tag{7}$$

Thus the *probability amplitudes* associated with the ''pattern dynamics'' evolve linearly over the time interval $\{t,t+\Delta t\}$, even though the *underlying dynamics* do not.

As an example, for a model with N independent, noninteracting segments, we have

$$\phi_n(\mathbf{x}_i)=\delta_{\mathrm{ni}}, \tag{8}$$

where δ_{ni} is the Kronecker symbol. Using Eqs. (5)–(8) for this case, we find an expression for $P(\mathbf{x}_i,t)$ that is identical to Eq. (4). The more interesting question arises when all of

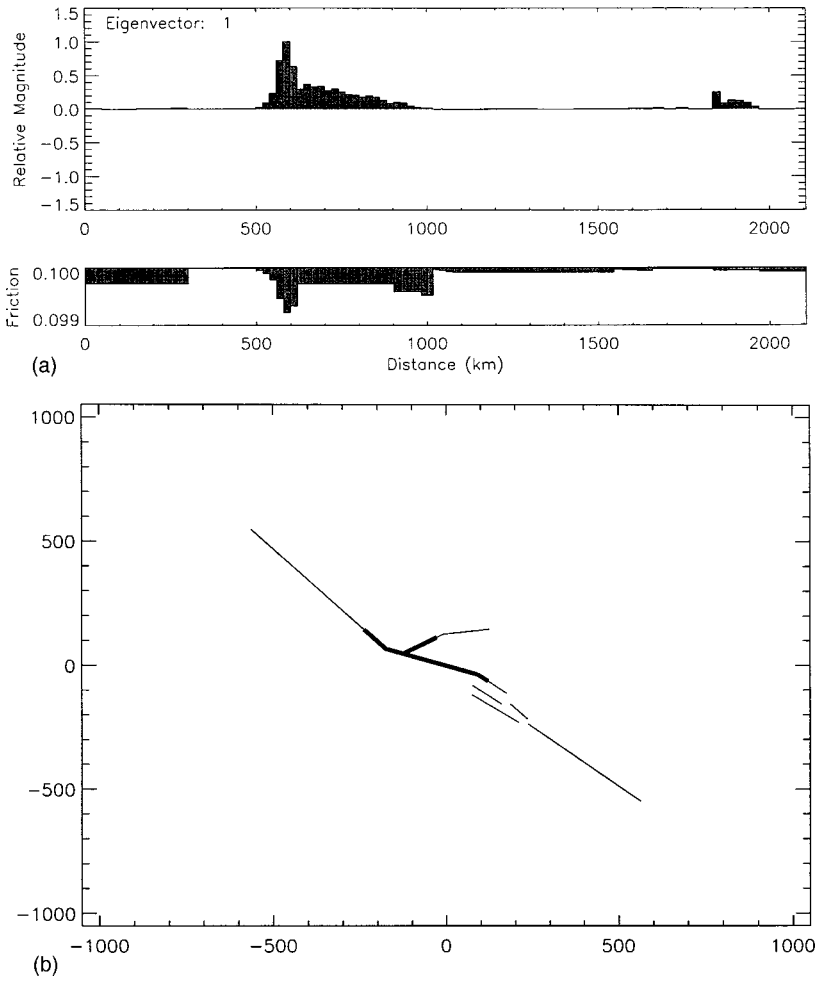

FIG. 5. Eigenvector ϕ_1. (a) Eigenvector plotted against distance. For display purposes, ϕ_1 are scaled so that $\max\{|\phi_1|\}=1$. (b) Map view. Values at all segments $\mathbf{x}_i$ at which $\phi_1(\mathbf{x}_i)>0.05$ are shown with a bold line. Values at all segments $\mathbf{x}_i$ at which $\phi_1(\mathbf{x}_i)<-0.05$ are shown with a dotted line. All other segments shown with a thin line. Period=804 years.

the segments or cells in a more general threshold system interact. In that case, it is not clear from the above discussion how the eigenvectors and eigenfrequencies can be computed. We address this topic in the following section.

IV. CORRELATION OPERATORS

When cells of a threshold system or other nonlinear system interact, it is likely that space-time correlations and patterns will develop (see, e.g., Refs. [10,49–51]). Correlations in the state variables $s(\mathbf{x},t)$ and $\sigma(\mathbf{x},t)$ lead to correlations in the firing activity pattern variables $\Psi(\mathbf{x},t)$. To describe the correlations in $\Psi(\mathbf{x},t)$, one can for example define any of a large number of equal time correlation operators. We consider two, a *static* correlation operator, and a *rate* correlation operator. The *static* correlation operator $C(\mathbf{x}_i,\mathbf{x}_j)$ between discrete sites at $\mathbf{x}_i$ and $\mathbf{x}_j$ is

$$C(\mathbf{x}_i,\mathbf{x}_j)\equiv\frac{1}{T}\int_0^T dt\, z(\mathbf{x}_i,t)z(\mathbf{x}_j,t), \tag{9}$$

where $z(\mathbf{x}_i,t)$ is the mean-zero, univariant time series obtained from the activity time series $\Psi(\mathbf{x}_i,t)$. The *rate* correlation operator $K(\mathbf{x}_i,\mathbf{x}_j)$ is

$$K(\mathbf{x}_i,\mathbf{x}_j)\equiv-\frac{1}{T}\int_0^T dt\,\frac{\partial z(\mathbf{x}_i,t)}{\partial t}\,\frac{\partial z(\mathbf{x}_j,t)}{\partial t}. \tag{10}$$

Both of the operators (9) and (10) are symmetric, rank-N matrix operators that can be diagonalized using standard methods. $C(\mathbf{x}_i,\mathbf{x}_j)$ is the Karhunen-Loeve operator [24,25,27] corresponding to the time series $z(\mathbf{x}_i,t)$. The eigenvalues of $C(\mathbf{x}_i,\mathbf{x}_j)$ represent relative probabilities p_n, with corresponding eigenvectors $\chi_n(\mathbf{x}_i)$. $K(\mathbf{x}_i,\mathbf{x}_j)$, however, is a new operator related to $C(\mathbf{x}_i,\mathbf{x}_j)$, involving the time series $\partial z(\mathbf{x}_i,t)/\partial t$. The eigenvalues of $K(\mathbf{x}_i,\mathbf{x}_j)$ are the squares of inverse times $(1/\tau_n)^2$, and are related to frequencies $\omega_n=2\pi/\tau_n$, with corresponding eigenvectors $\phi_n(\mathbf{x}_i)$. The latter are just the eigenfrequencies and eigenvectors that we use to define the reconstructed pattern state $\Psi_R(\mathbf{x}_i,t)$ in Eq. (5). In Appendix A, we discuss the physical significance of the eigenvalues of $K(\mathbf{x}_i,\mathbf{x}_j)$.

Other correlation operators could be defined as well. For example, one can define a time series $y(\mathbf{x}_i,t)$ whose entries are the slip on segment $\mathbf{x}_i$ in the time interval $\{t,t+\Delta t\}$ and whose eigenvalues have the units of slip squared. Or one can define a time series $w(\mathbf{x}_i,t)$ whose entries are the number of events and whose eigenvalues are the squares of relative frequencies. Or one can define a covariance matrix if $z(\mathbf{x}_i,t)$ is

not univariant, and so forth. Any of these possible operators can be examined using the methods we describe, some of which we are in the process of studying. Each yields different information about correlations in the patterns and the processes in the system. The eigenvectors of each contain information related to the spatial correlations between segments.

Since $\Psi(\mathbf{x}_i,t)$ and $z(\mathbf{x}_i,t)$ represent time series whose elements are impulse functions, it is operationally difficult to compute the time derivatives in Eq. (10). Computing $K(\mathbf{x}_i,\mathbf{x}_j)$ is therefore difficult, whereas computing $C(\mathbf{x}_i,\mathbf{x}_j)$ is easy. As a result, we propose an alternative approach based on Fourier transforms:

$$z(\mathbf{x}_i,t)=\frac{1}{\sqrt{2\pi}}\int_{-\infty}^{\infty}d\varpi_i\, e^{i\bar{\omega}_i t}\hat{z}(\mathbf{x}_i,\varpi_i). \tag{11}$$

Then,

$$C(\mathbf{x}_i,\mathbf{x}_j)=\int_{-\infty}^{\infty}\int_{-\infty}^{\infty}d\varpi_i d\varpi_j P_*(\mathbf{x}_i,\mathbf{x}_j,\varpi_i,\varpi_j), \tag{12}$$

$$K(\mathbf{x}_i,\mathbf{x}_j)=\int_{-\infty}^{\infty}\int_{-\infty}^{\infty}d\varpi_i d\varpi_j \varpi_i\varpi_j P_*(\mathbf{x}_i,\mathbf{x}_j,\varpi_i,\varpi_j). \tag{13}$$

$P_*(\mathbf{x}_i,\mathbf{x}_j,\varpi_i,\varpi_j)$ is the joint probability density of the two variables ϖ_i, ϖ_j:

$$P_*(\mathbf{x}_i,\mathbf{x}_j,\varpi_i,\varpi_j)=\hat{z}(\mathbf{x}_i,\varpi_i)\hat{z}(\mathbf{x}_j,\varpi_j)\times\left\{\frac{1}{2\pi T}\int_0^T dt\, e^{i(\varpi_i+\varpi_j)t}\right\}. \tag{14}$$

The covariance $\langle\varpi_i\varpi_j\rangle$ is then

$$\left\langle \varpi_i\varpi_j=\frac{\int_{-\infty}^{\infty}\int_{-\infty}^{\infty}d\varpi_i d\varpi_j\varpi_i\varpi_j P_*(\mathbf{x}_i,\mathbf{x}_j,\varpi_i,\varpi_j)}{\int_{-\infty}^{\infty}\int_{-\infty}^{\infty}d\varpi_i d\varpi_j P_*(\mathbf{x}_i,\mathbf{x}_j,\varpi_i,\varpi_j)}\right. . \tag{15}$$

If we assume that the joint spectra of the time series are simultaneously sharply peaked about the average frequencies $\langle\varpi_i\rangle$ and $\langle\varpi_j\rangle$,

$$\left|\frac{\langle(\varpi_i-\langle\varpi_i\rangle)(\varpi_j-\langle\varpi_j\rangle)\rangle}{\langle\varpi_i\rangle\langle\varpi_j\rangle}\right|\ll 1, \tag{16}$$

we obtain the result

$$K(\mathbf{x}_i,\mathbf{x}_j)\approx C(\mathbf{x}_i,\mathbf{x}_j)\langle\varpi_i\rangle\langle\varpi_j\rangle. \tag{17}$$

The frequencies $\langle\varpi_i\rangle$ are observables, they are simply

$$\langle\varpi_i\rangle=\pi\nu_i \tag{18}$$

from Eq. (3).

Once $K(\mathbf{x}_i,\mathbf{x}_j)$ is found from Eq. (17), it can be diagonalized to obtain the normal modes of the patterns, the eigenfrequencies ω_n and the eigenvectors $\phi_n(\mathbf{x}_i)$. The eigenvectors provide information about specific patterns of spatial correlations between sites, and the eigenfrequencies provide information about how often these recur. $\phi_n(\mathbf{x}_i)$ and ω_n can be inserted into Eq. (5) to obtain $\Psi_R(\mathbf{x}_i,t)$; then forecast probabilities $P(\mathbf{x}_i,t)$ can be computed using Eq. (7).

V. FORECAST METHODOLOGY

Our forecast methodology makes use of Eqs. (5)–(7). Given an observed pattern $\Psi(\mathbf{x},t)$, we wish to compute $P(\mathbf{x}_i,t+\Delta t)$, the probability density for ''firing'' activity at the next time step. From Eq. (6) we have

$$\Psi_{\rm obs}(\mathbf{x}_i,t)=\frac{1}{\sqrt{2}}\{\Psi_R(\mathbf{x}_i,t)+\Psi_R^*(\mathbf{x}_i,t)\}$$

$$=\sum_{n=1,N}\beta_n\cos\{\omega_n t\}\phi_n(\mathbf{x}_i). \tag{19}$$

Our approach is to use the observed pattern data $\Psi(\mathbf{x},t)$ prior to $t+\Delta t$ to find $\phi_n(\mathbf{x}_i)$ and ω_n from the operator $K(\mathbf{x}_i,\mathbf{x}_j)$. Furthermore, if the β_n are known, Eq. (6) can then be used to compute $P(\mathbf{x}_i,t+\Delta t)$:

$$P(\mathbf{x}_i,t+\Delta t)=|\Psi_{\rm obs}(\mathbf{x}_i,t+\Delta t)|^2=\{\Psi_{\rm obs}(\mathbf{x}_i,t+\Delta t)\}^2. \tag{20}$$

To fix the N values β_n in Eq. (19), we find the most recent time t_{mi} prior to time t at which the segment or cell at $\mathbf{x}_i$ ''fires.'' We then require that

$$\Psi_{\rm obs}(\mathbf{x}_i,t_{0i})=(-1)^m. \tag{21}$$

Here m represents the index of each event at site $\mathbf{x}_i$, with the first event being $m=0$, the next event being $m=1$, and so forth. Condition (21) then leads to a set of $N\times N$ independent equations that can be solved by standard methods. This entire process is then repeated in an iterative mode to calculate $P(\mathbf{x}_i,t+2\Delta t)$, and so forth, always taking care to use the most recent data to calculate the β_n.

VI. APPLICATION: PATTERNS IN NUMERICAL SIMULATIONS OF EARTHQUAKES

As an illustration of the points discussed above, we used these methods to calculate the probability of activity on a realistic model of an earthquake fault system. Details of this model are described in Appendix B.

Simulations totaling tens of thousands of model years were carried out. In Fig. 2, we show a time-distance plot of all the events occurring in 2000 years of simulation data after all initial transients have died away, with a reference map view of the model fault system. Figure 3 shows the events at year 21 664, and in Fig. 4, the events at year 22 554. The data shown in Fig. 2 (top) were used to construct $C(\mathbf{x}_i,\mathbf{x}_j)$ and $K(\mathbf{x}_i,\mathbf{x}_j)$, from which were obtained the eigenvectors $\phi_n(\mathbf{x})$ and eigenfrequencies ω_n. The first three spatial eigenvectors for the 6000-year time period preceding the data shown in Fig. 2 are shown in Figs. 5–7. It is interesting that between distances ~500 km to ~1000 km, the eigenvector in Fig. 5 has 0 spatial nodes, the eigenvector in Fig. 6 has one spatial node, and the eigenvector in Fig. 7 has two spatial nodes. From the completeness and orthonormality of the eigenvectors in the pattern basis set, it can easily be shown that any

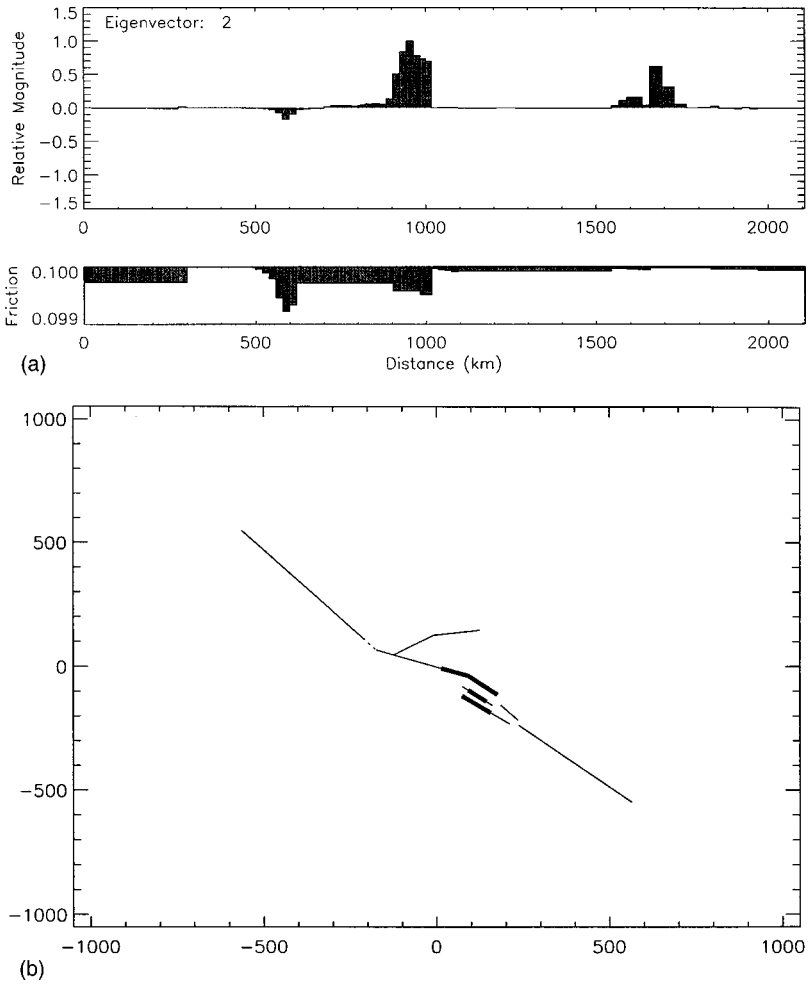

FIG. 6. Eigenvector ϕ_2, as in Figs. 5(a) and 5(b). Period=680 years.

pattern of slip probability amplitude (e.g., $=\pm 1$ where fault segment slips; $=0$ where fault segment is quiescent) can be reproduced by superposition of the appropriate eigenvectors.

Using the methods outlined above, the probability $P(\mathbf{x}_i,t)$ for fault segment $\mathbf{x}_i$ to slip at time t was computed. The eigenstates and eigenperiods were obtained from a simulation data set over the 6000 years prior to the data to be predicted (''training data set''), so as to minimize biases. The results are shown in Fig. 8, which shows a 300-year subset of simulation data taken from that shown in Fig. 2. Figure 8 also shows contours of probability $P(\mathbf{x}_i,t)$ superposed on the previous simulation data. It can be seen that in many cases, there is reasonable agreement between probabilities and the time and location of events, although the ''false alarm'' rate is high.

VII. ''RANDOMIZED MODEL'' AND UNCERTAINTY PRINCIPLE

Success in forecasting future events using the pattern dynamics method depends on the capability of accurately retrieving both the eigenvectors $\phi_n(\mathbf{x}_i)$ and the eigenfrequencies ω_i. For purposes of comparison, it is useful to have an alternative model, which we call the ''randomized model,'' which illuminates trade-offs in different approaches. This new model defines the eigenfrequencies at each site much more precisely, but at the expense of losing important information about the spatial correlation patterns.

The impulsive time series defining the correlation operators consist of signals that are sharply localized in time. However, time series having signals localized in time have a relatively flat spectrum over a broad range of frequencies. The uncertainty principle for Fourier transforms [28] defined using Eq. (23) indicates that

$$\{\langle \Delta\omega\rangle\langle \Delta t\rangle\} \geqslant \pi. \tag{22}$$

This result suggests a simple but illustrative strategy to improve the frequency resolution of the method described above: that we add a random time increment, drawn from a uniform distribution of times about the original firing time, to each firing time of the $y_i(t_m)$. In this way, we degrade the temporal resolution without changing the average frequency ν_i or the mean firing time. We should then expect that resolution of normal mode frequencies will improve. However, as remarked above, important information will be lost about the spatial correlations of the various sites.

To test this idea, we defined a set of new random time series $y_i'(t_m)$, in which the time of each firing was altered by the addition of a random number uniformly distributed on the interval $[-1/2\nu_i, +1/2\nu_i]$. Because the randomized times are uniformly distributed around the original firing

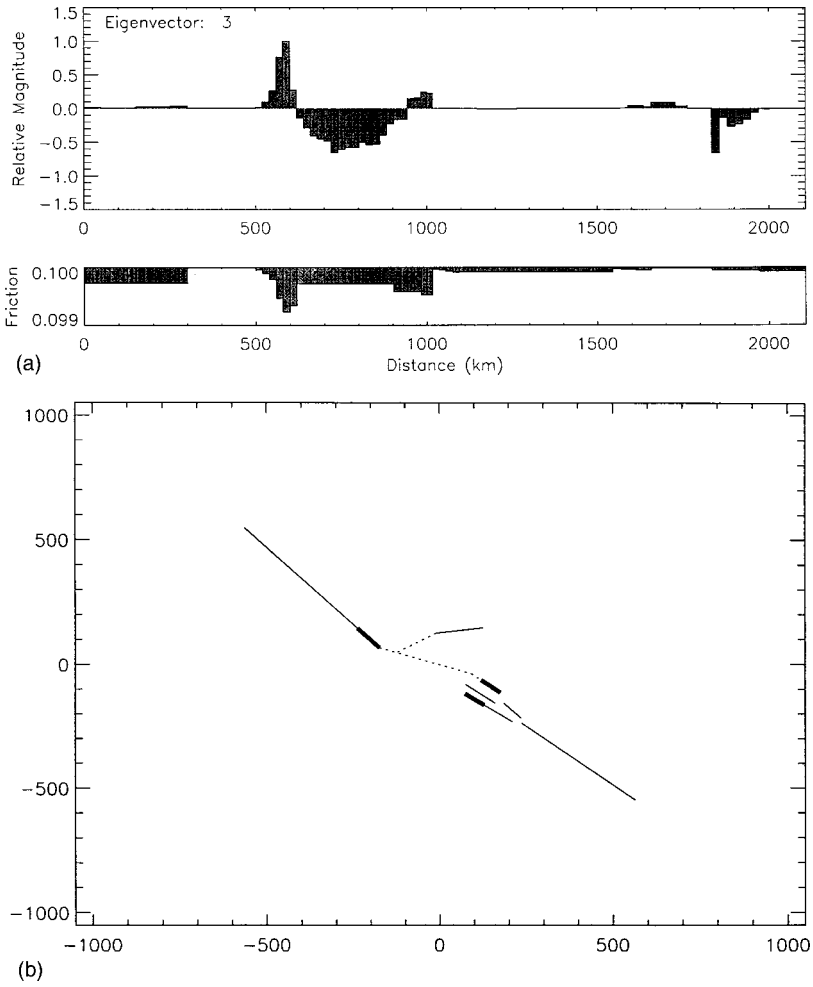

FIG. 7. Eigenvector ϕ_3, as in Figs. 5(a) and 5(b). Period=597 years.

times, a memory of the original firing times is retained. We then repeated the entire procedure and constructed new forecast probabilities $P(\mathbf{x}_i,t)$. The eigenvectors corresponding to the three largest eigenvalues are shown in Figs. 9–11. It can be seen from these figures that better frequency resolution is obtained at the cost of obtaining less knowledge about spatial correlations between sites $\mathbf{x}_i$ and $\mathbf{x}_j$. It is important to note that this ''randomized'' model is not the only means of

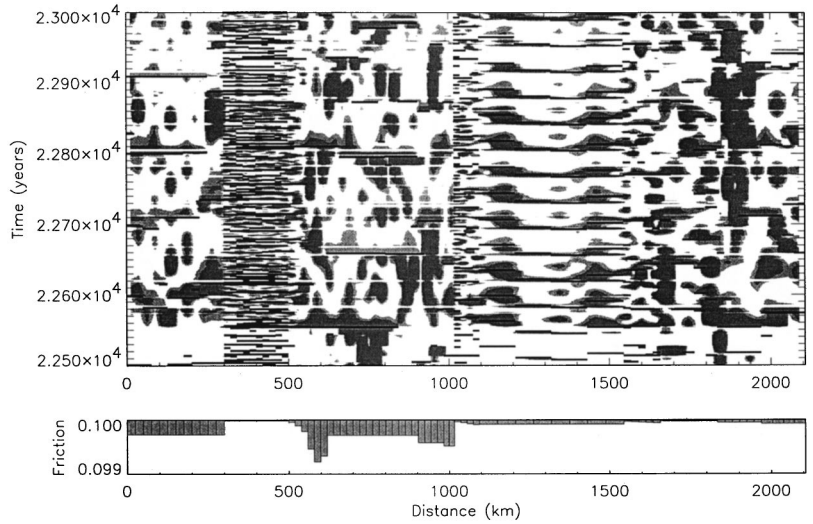

FIG. 8. Superposition of events (solid horizontal lines) from year 22 500 to year 23 000 top with probabilities $P(\mathbf{x}_i,t)$ calculated according to Eq. (20). Light shaded regions are for $P(\mathbf{x}_i,t)>1/3$; dark shaded regions are for $P(\mathbf{x}_i,t)>1/2$. The method used was the basic method described in Sec. V.

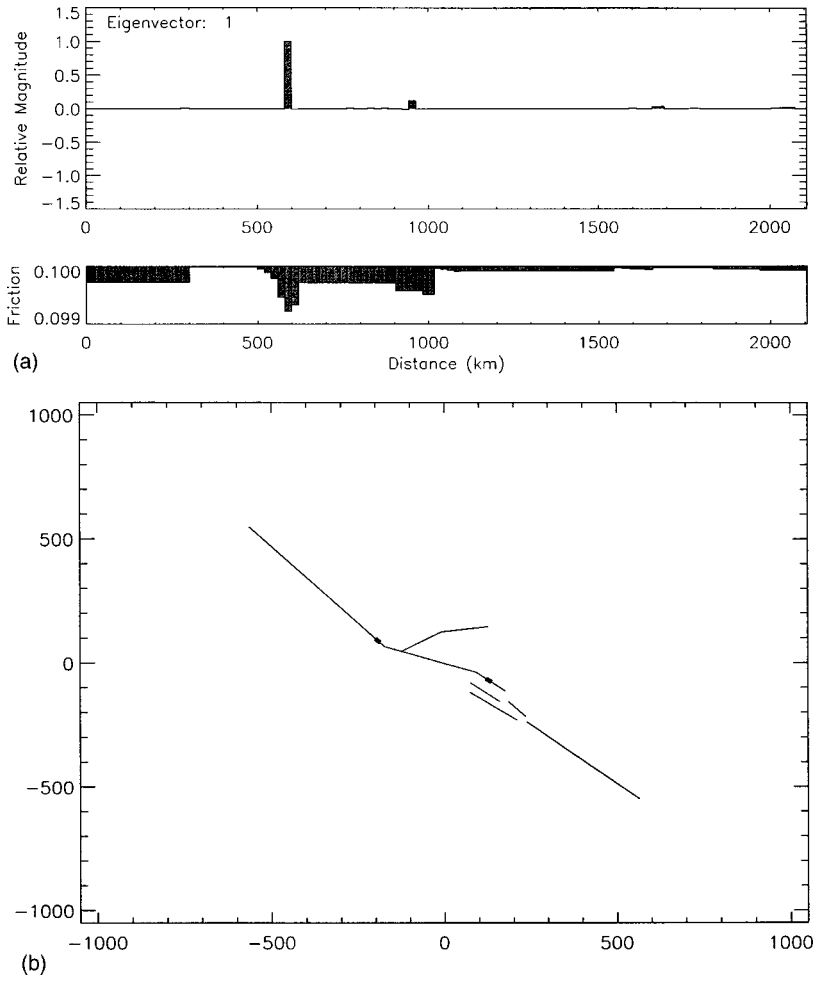

FIG. 9. Eigenvector ϕ_1 for randomized model, as in Figs. 5(a) and 5(b). Period=580 years.

trading frequency for spatial information, but has the virtue of being simple and illustrative, which is what we require here. Other methods, for example, those based on wavelets [24] have been discussed extensively elsewhere. We discuss other methods in a separate publication [52].

Results for the new forecast probabilities are shown in Fig. 12 for the same simulation data as was used in Fig. 8. In several locations; for example, at distances ranging from 0 to 300 km, and from 500 to 1000 km, forecasts in Fig. 12 are superior to those in Fig. 8. However, the likelihood ratio test described below indicates that the original method with nonrandomized times is more accurate overall.

VIII. STATISTICAL TEST OF FORECAST PROBABILITIES

The method we describe can be tested by statistical means to assess the quality of the forecast. The predictive skill of a proposed method can be compared, for example, to a standard Poisson model by computing a likelihood ratio. The same method has been used to evaluate other proposed forecast methods, including time-to-failure models, for real earthquakes [39]. The likelihood test is based on the idea that a cost is incurred if a forecast method produces a false alarm, i.e., an event during a time interval when no event occurs. Using this test, we find that the pattern dynamics (PD) method associates significantly more probability measure with the actual simulation events than does a competing Poisson probability model.

The likelihood ratio method is described in detail elsewhere [39], and only a brief summary is given here. Consider a given normalized probability density $P(\mathbf{x},t)$. If the ith of N fault segments slips Q_i times, so that there are N_T total events on all segments, the likelihood function is

$$L=\prod_{i=1}^{N_T}\prod_{q=1}^{Q_i} P(\mathbf{x}_i,t_q). \tag{23}$$

We wish to compare the quality of forecasts given by two probability distributions; for example, the PD method $P_{\mathrm{PD}}(\mathbf{x}_i t)$ and a reference time-independent Poisson model $P_p(\mathbf{x})$. The corresponding likelihoods are designated as L_{PD} and L_P. To compare the two probability models, we define a composite likelihood ratio that involves a mixing ratio r:

$$L(r)=\prod_{i=1}^{N_T}\prod_{q=1}^{Q_i} P(\mathbf{x}_i,t_q,r), \tag{24}$$

where

$$P(\mathbf{x}_i,t_q,r)=rP_{\mathrm{PD}}(\mathbf{x}_i,t_q)+(1-r)P_p(\mathbf{x}_i). \tag{25}$$

Equations (23)–(25) assumes that the earthquakes are all statistically independent, a standard assumption that is clearly

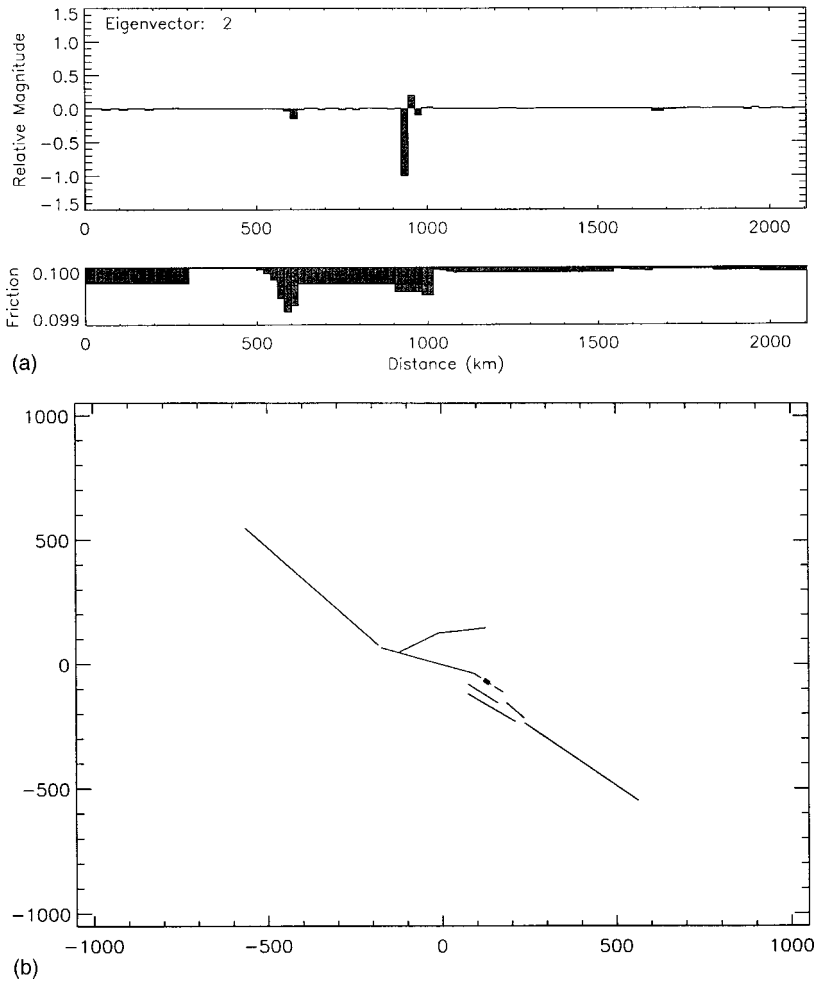

FIG. 10. Eigenvector ϕ_2 for randomized model, as in Figs. 5(a) and 5(b). Period=476 years.

not correct in the case of our simulations. However, statistical independence is an assumption routinely used in earthquake forecasting, and the Poisson model represents one of the current most widely used method for calculating an earthquake hazard [3,39].

Significance of results. In Fig. 13, we plot the log-likelihood ratio $\log_{10}\{L_R(r)\}$, which is defined by

$$\log_{10}\{L_R(r)\}=\log_{10}\left\{\frac{L(r)}{L_p}\right\}$$
$$=\log_{10}\{L(r)\}-\log_{10}\{L_p\}. \qquad (26)$$

Likelihoods must be interpreted only by comparing probability models fit to exactly the same data. In Fig. 13, we show a plot of $\log_{10}\{L_R(r)\}$ against the mixing ratio r, corresponding to the forecasts and simulation data in Figs. 8 and 12. In both cases

$$L(r)\gg L_P, \quad r>0, \qquad (27)$$

implying that $L_{\rm PD}\gg L_P$. These results show that the PD model is substantially better ($\sim$20 in Fig. 8, $\sim$5 in Fig. 13 for large r) than the Poisson model at predicting the occurrence times and locations of the synthetic events. The best probability models for both randomized and nonrandomized forecasts are those with the largest r. Cases with $r=1$ cannot be evaluated: if an event were not predicted, $P_{\rm PD}(\mathbf{x}_i,t_q)=0$ there. Since $L_{\rm PD}$ is a product of all the probabilities $P_{\rm PD}(\mathbf{x}_i,t_q)$ at the times and locations of the events, $L_{\rm PD}$ would be zero, and $\log_{10}\{L_{\rm PD}\}$ would be undefined.

From examination of Figs. 8 and 13, it can be seen that there exist a number of false positive space-time forecasts in using the probability model $P_{\rm PD}(\mathbf{x}_i,t_m)$, as well as some ''failures to predict.'' However, the result (27) means that $P_{\rm PD}(\mathbf{x},t)$ still puts far more of its probability measure at the times of the slip events than does $P_P(\mathbf{x})$.

IX. FINAL COMMENTS

A variety of methods have been proposed for understanding the space-time patterns in driven nonlinear systems including principal component analysis [26,31], principal oscillation pattern [27–29] analysis, and singular spectrum analysis [25,32,33]. However, in these systems, the variables that define the underlying dynamics are directly amenable to observation, in contrast to most driven threshold systems, such as neural systems, earthquakes, and disordered magnetic systems. In these driven threshold systems, only the associated ''derivative variables,'' such as the correlated firing activity or earthquakes, can be directly observed. Thus the standard methods cannot be applied to threshold systems without serious qualifications. Other methods that are being

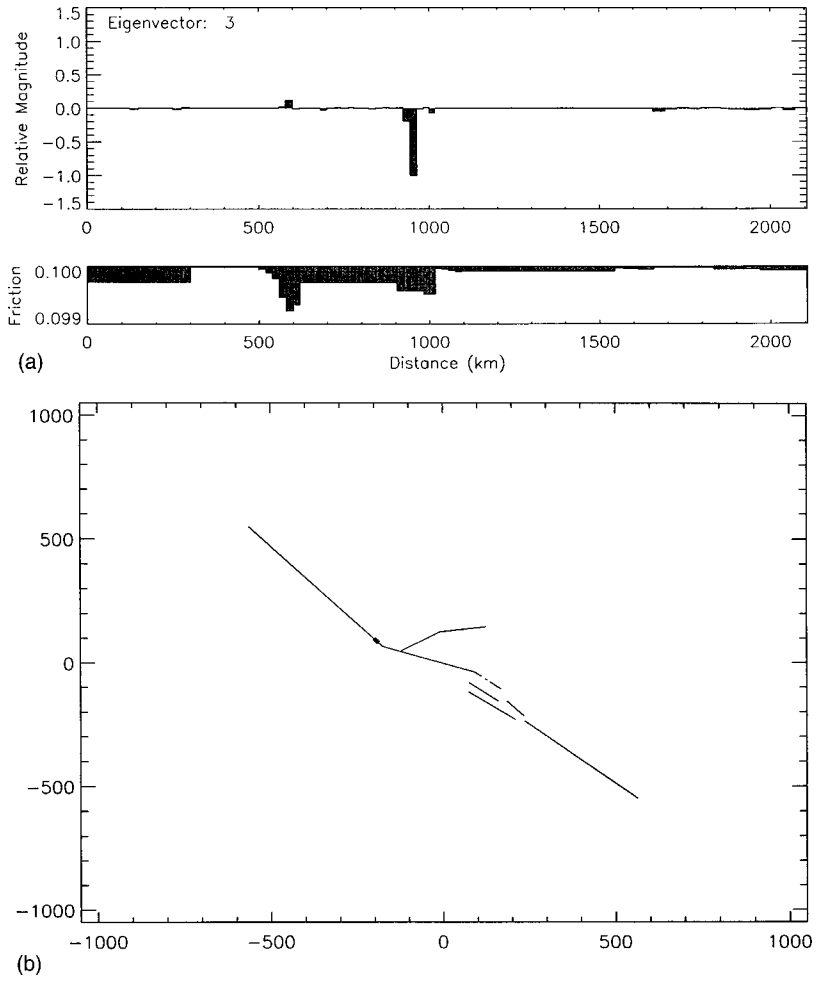

FIG. 11. Eigenvector ϕ_3 for randomized model, as in Figs. 5(a) and 5(b). Period=473 years.

examined elsewhere are described in Refs. [41–48,50,51], but these have so far not yielded adequate results for threshold systems. Applications of our methods to observed seismicity data taken from real fault systems will be given elsewhere [52].

Understanding the patterns of firings in nonlinear threshold systems must proceed via the construction of representative simulations and the development of analysis methods for the patterns that result. Once the analysis methods are in place, they should be applied to forecasting and understand-

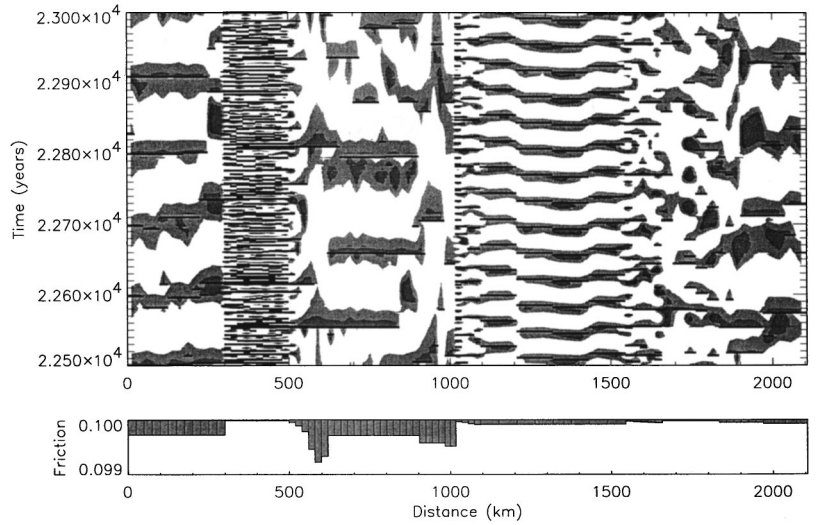

FIG. 12. Superposition of events (solid horizontal lines) from year 22 500 to year 23 000 top with probabilities $P(\mathbf{x}_i,t)$ calculated according to Eq. (20) using ''improvements'' described in Sec. VII. Light shaded regions are for $P(\mathbf{x}_i,t)>1/3$; dark shaded regions are for $P(\mathbf{x}_i,t)>1/2$.

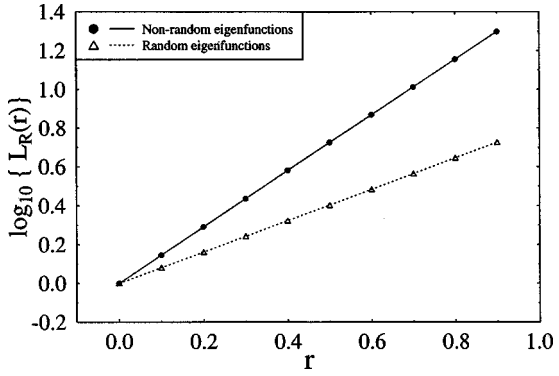

FIG. 13. Plot of log-likelihood ratio $\log_{10}\{L_R(r)\}$ against mixing ratio r corresponding to event forecasts in Figs. 8 (solid, circles) and 12 (dashed, triangles).

ing data from natural systems. In particular, it is often the case that the largest correlated-firing events are the most infrequent, but the most important to understand, since they usually act to slave the entire system. For earthquake models, these correspond to the largest and most destructive events. Detailed pattern analysis may allow the patterns of smaller, more frequent events leading up to the largest events to be detected and recognized. If this can be demonstrated, reliable forecasting of the largest events may be possible.

ACKNOWLEDGMENTS

The authors would like to acknowledge helpful conversations with C. Penland, J. Hopfield, Marian Anghel, J. de sa Martins, J. Perez-Mercader, and Murray Gell-Mann. We wish to thank D. Sornette for careful and thoughtful comments. Research by J.B.R. was supported by NASA under Grant No. NAG5-5168 (simulations), and by the US DOE Grant No. DE-FG03-95ER14499 (theory) to the University of Colorado. Research by W.K. was supported by the US DOE through Grant No. DE-FG02-95ER14498 to Boston University. Research by K.T. was supported by NASA under Grant No. NGT5-30025.

APPENDIX A: EIGENVALUES OF $K(\mathbf{x}_i,\mathbf{x}_j)$

In this appendix we give an argument as to why the eigenvalues of the rate correlation matrix $K(\mathbf{x}_i,\mathbf{x}_j)$ should equal the square of the frequencies of the eigenmodes. The main assumptions we make for this illustration is that each fault segment that can fail has only one frequency, and that the time averaging period can be approximated by infinity.

Consider first the simple case where each fault segment has a different frequency ϖ_i in the Fourier domain. Referring to Eq. (11), we can represent each time series as

$$z(\mathbf{x}_i,t)=\mathrm{Re}\{z(\mathbf{x}_j,0)e^{i\overline{\omega}_j t}\}. \tag{A1}$$

In this case, with normalization, the static correlation matrix is the identity matrix. The rate correlation matrix is also diagonal with elements of ϖ_i^2. Consequently, in this simple case the eigenvectors of the static correlation matrix and the rate correlation matrix are the same, and the eigenvalues of the rate matrix are simply the frequencies.

In the slightly more complicated case where the frequencies can be the same the matrices are no longer diagonal. However, it is simple to see that any two rows have the following property: either they are identical or they are disjoint. By disjoint we mean that the nonzero elements in one row, say row 1, are zero in any other row that is not identical to row 1. Since the numbering of the fault segments is arbitrary, we can renumber so that all of the rows that are identical are grouped together. This will put the matrices in Jordan-normal form. That is, the matrices, both static and rate correlation, are now made up of blocks of nonzero elements arranged along the diagonal. Each block has the same nonzero element, which is simply the frequency squared of some element in the rate correlation matrix and one in the static matrix. Clearly, the eigenvalues of the rate matrix are the square of the frequencies times the eigenvalues of the static matrix.

In the case of real data, it is certainly true that the time-averaging period is not infinite and the number of frequencies for an individual fault element is not 1. However, there is evidence that we discussed in the body of the paper that supports the point of view that the assumptions we made are good approximations. It is clear that there will be modifications that will need to be made to incorporate additional modes and finite averaging times if we wish to forecast over long times, and that the less periodic the individual fault elements are, the more important the corrections will be.

APPENDIX B: EARTHQUAKE FAULT SYSTEM MODEL

A particularly complicated example of space-time patterns in a nonlinear threshold system arises in the dynamical model of the earthquake fault system described in Ref. [34]. In contrast to many current models in the literature describing a single planar fault, the model in Ref. [34] includes all of the major faults in southern California, albeit at a relatively crude scale (Fig. 2, bottom). In this cellular automaton-type model, each of $N=80$ fault segments is driven at its own particular long-term rate V of a few centimeters/year.

Segment i slips when the shear stress $\sigma_{\mathrm{sb},i}(t)=\mu_s\sigma_{\mathrm{norm},i}(t)$, where μ_s is a preassigned coefficient of ''static'' friction, and $\sigma_{\mathrm{norm},i}(t)$ is the normal stress on the segment. At failure, slip occurs that is sufficient to reduce $\sigma_{\mathrm{sh},i}(t)$ to the value $\sigma_{\mathrm{sh},i}(t)=\mu_d\sigma_{\mathrm{norm},i}(t)$, where μ_d is a coefficient of ''dynamic'' friction. The difference in frictional coefficients $\mu_s-\mu_d$ is tuned so that realistic event sequences on the middle (''big bend'') and southern parts of the model San Andreas fault occur at realistic intervals of $\sim$150 years. Some tuning was also carried out to produce ''realistic'' sequences on the Imperial, the San Jacinto, the Elsinore, and Garlock faults, in contrast to frictional properties on the Cerro Prieto and Northern San Andreas fault segments, which were not tuned. Time steps of one year are used. Interactions between segments allow stress transfer so that one slipping sement can induce others to slip as well in the same event. Realistic directionally dependent elastic and viscoelastic interactions are included by means of the stress Green's functions. In Fig. 2 (bottom) we show a map view of the 80 segments of the model, each of which is a vertical rectangular slip surface. These segments extend to a depth of 18 km in an elastic plate of thickness 30 km. The plate overlies, and is in welded contact with, a Maxwell viscoelastic half space in which shear stress can relax via viscoelastic flow. The reader is referred to Ref. [34] for other details.

[1] J. B. Rundle and W. Klein, Rev. Geophys. Space Phys. **July**, 283 (1995).
[2] D. S. Fisher, K. Dahmen, S. Ramanathan and Y. Ben-Zion, Phys. Rev. Lett. **78**, 4885 (1997).
[3] C. H. Scholz, *The Mechanics of Earthquakes and Faulting* (Cambridge University Press, Cambridge, UK, 1990).
[4] J. Hertz, A. Korgh and R. G. Palmer, *Introduction to the Theory of Neural Computation*, Lecture Notes I, Santa Fe Institute (Addison Wesley, Reading, MA, 1991).
[5] A. V. M. Herz and J. J. Hopfield, Phys. Rev. Lett. **75**, 1222 (1995).
[6] D. S. Fisher, Phys. Rev. B **31**, 1396 (1985).
[7] J. S. Urbach, R. C. Madison, and J. T. Markert, Phys. Rev. Lett. **75**, 276 (1995).
[8] P. Bak, C. Tang and K. Weisenfield, Phys. Rev. Lett. **59**, 381 (1987).
[9] A. D. Gopal and D. J. Durian, Phys. Rev. Lett. **75**, 2610 (1995).
[10] *Pattern Formation in the Physical and Biological Sciences*, edited by H. F. Nijhout, L. Nadel, and D. L. Stein, Lecture Notes V, Santa Fe Institute (Addison Wesley, Reading, MA, 1997).
[11] C. M. Gray, in *Pattern Formation in the Physical and Biological Sciences* (Ref. [10]), p. 93.
[12] C. J. Shatz, in *Pattern Formation in the Physical and Biological Sciences* (Ref. [10]), p. 299.
[13] M. Constantine-Paton, H. T. Cline, and E. Debski, Annu. Rev. Neurosci. **13**, 129 (1990).
[14] M. Abeles, *Corticonics, Neural Circuts of the Cerebral Cortex* (Cambridge University Press, Cambridge, UK, 1991).
[15] D. Hill, J. P. Eaton, and L. M. Jones, in *The San Andreas Fault System, California*, edited by R. E. Wallace, U.S. Geol. Surv. Prof. Paper 1515 (U.S. GPO, Washington, DC, 1990).
[16] K. Sieh, M. Stuiver, and D. Brillinger, J. Geophys. Res. **94**, 603 (1989).
[17] W. Bakun and T. V. McEvilly, J. Geophys. Res. **89**, 3051 (1984).
[18] H. Haken, *Synergetics, An Introduction* (Springer-Verlag, Berlin, 1983).
[19] C. W. Gardiner, *Handbook of Stochastic Methods* (Springer-Verlag, Berlin, 1985).
[20] J. B. Rundle, W. Klein, S. Gross, and D. L. Turcotte, Phys. Rev. Lett. **75**, 1658 (1995).
[21] W. Klein, J. B. Rundle, and C. Ferguson, Phys. Rev. Lett. **78**, 3793 (1997).
[22] C. D. Ferguson, W. Klein and J. B. Rundle, Phys. Rev. E (to be published).
[23] K. Huang, *Statistical Mechanics* (John Wiley, New York, 1987).
[24] P. J. Holmes, J. L. Lumley, and G. Berkooz, *Turbulence, Coherent Structures, Dynamical Systems and Symmetry* (Cambridge University Press, Cambridge, UK, 1996).
[25] K. Fukunaga, *Introduction to Statistical Pattern Recognition* (Academic Press, New York, 1990); see especially Chap. 9.
[26] H. Hotelling, J. Educ. Psych. **24**, 417 (1933).
[27] R. W. Preisendorfer, *Principal Component Analysis in Meteorology and Oceanography*, edited by C. D. Mobley, Develop. Atm. Sci. (Elsevier, Amsterdam, 1988), Vol. 17.
[28] C. Penland, Mon. Weather Rev. **117**, 2165 (1989).
[29] A. Garcia and C. Penland, J. Stat. Phys. **64**, 1121 (1991).
[30] C. Penland and P. D. Sardeshmukh, J. Clim. **8**, 1999 (1995).
[31] C. Penland and T. Magorian, J. Clim. **6**, 1067 (1993).
[32] D. S. Broomhead and G. P. King, Physica D **20**, 217 (1986).
[33] R. Vautard and M. Ghil, Physica D **35**, 395 (1989).
[34] J. B. Rundle, J. Geophys. Res. **93**, 6255 (1988).
[35] Y. Y. Kagan and D. D. Jackson, Geophys. J. Int. **104**, 117 (1991).
[36] S. Gross and C. Kisslinger, Bull. Seismol. Soc. Am. **84**, 1571 (1994).
[37] J. B. Rundle, W. Klein, and S. Gross, in *Reduction and Predictability of Natural Hazards*, Santa Fe. Inst. Ser. Sci. Complexity (Addision-Wesley, Reading, MA., 1996), Vol. 25.
[38] D. Sornette and L. Knopoff, Bull. Seismol. Soc. Am. **87**, 789 (1997).
[39] S. Gross and J. B. Rundle, Geophys. J. Int. **133**, 57 (1998).
[40] J. P. Crutchfield and J. F. Hanson, Physica D **69**, 279 (1993).
[41] M. Eneva and Y. Ben-Zion, J. Geophys. Res. **102**, 24 513 (1997).
[42] M. Eneva and Y. Ben-Zion, J. Geophys. Res. **102**, 17 785 (1997).
[43] S. L. Pepke and J. M. Carlson, Phys. Rev. E **50**, 236 (1994).
[44] S. L. Pepke, J. M. Carlson, and B. E. Shaw, J. Geophys. Res. **99**, 6769 (1994).
[45] V. Kossobokov and J. M. Carlson, J. Geophys. Res. **100**, 6431 (1995).
[46] J.-B. Minster and N. Williams, Trans., Am. Geophys. Union **73(43)**, 366 (1992).
[47] G. M. Molchan and Y. Y. Kagan, J. Geophys. Res. **97**, 4823 (1992).
[48] C. G. Sammis, D. Sornette, and H. Saleur, in *Reduction and Predictability of Natural Hazards*, (Ref. [37]), pp. 143–156.
[49] P. Ball, *The Self-Made Tapestry, Pattern Formation in Nature* (Oxford University Press, Oxford, UK, 1999).
[50] T. Ouchi, Pure Appl. Geophys. **140**, 15 (1993).
[51] T. Ouchi (unpublished).
[52] K. Tiampo, J. B. Rundle, and W. Klein (unpublished).